Measurement 256 (2025) 118214

Contents lists available at ScienceDirect

Measurement

journal homepage: www.elsevier.com/locate/measurement

Demodulation method for heterodyne Φ-OTDR with fading noise suppression based on Fourier transform and spatial-temporal phase compensation

Hao Ding [a,b], Xuping Zhang [a,b], Shaoxiong Tang [a,b], Qiming Deng [a,b], Chi Zhang [a,b], Shuai Tong [a,b], Yixin Zhang [a,b,*], Huanhuan Liu [c], Fei Xiong [d], Ningmu Zou [a,e,*]

[a] *Key Laboratory of Intelligent Optical Sensing and Manipulation, Ministry of Education, Nanjing University, Nanjing 210093, China*
[b] *College of Engineering and Applied Sciences, Nanjing University, Nanjing 210023, China*
[c] *Shenzhen Institute of Advanced Technology, Chinese Academy of Sciences, Shenzhen 518055, China*
[d] *Inner Mongolia DT Electric Power Design, Hohhot 010010, China*
[e] *School of Integrated Circuits, Nanjing University, Suzhou 215163, China*

ARTICLE INFO

Keywords:
Optical fiber sensing
Φ-OTDR
Phase demodulation
Fading suppression

ABSTRACT

The heterodyne phase-sensitive optical time-domain reflectometry (Φ-OTDR) technique has been widely applied in various fields. In this context, we propose a digital phase demodulation algorithm, FTM-STPC, which efficiently integrates fading noise suppression directly into heterodyne Φ-OTDR systems, thus eliminating the need for additional phase demodulation and noise suppression hardware modules. Diverging from traditional digital coherent demodulation methods, FTM-STPC optimizes the phase demodulation process by utilizing frequency domain processing instead of generating digital orthogonal signals and digital time-domain filters. This approach not only improves phase information fidelity through adaptive filtering but also precisely identifies fading points by detecting residues and employs Spatial-Temporal Phase Compensation (STPC) for effective fading noise suppression under challenging conditions. Simulation and experimental results confirm that, compared to traditional digital I/Q phase demodulation, the proposed FTM-STPC achieves improvements in demodulation speed, accuracy, and noise resistance, while reducing fading noise suppression to below 1%.

1. Introduction

Since the phase-sensitive optical time-domain reflectometry (Φ-OTDR) was first proposed in 1993, it has emerged as an essential tool in distributed sensing [1]. Renowned for its ability to accurately localize disturbances along optical fibers and reconstruct multidimensional signal characteristics for the events of interesting, including amplitude, phase, and frequency [2]. In Φ-OTDR systems, phase demodulation is pivotal, significantly influencing performance, complexity, and cost. Various optimization techniques have been developed, including 3 × 3 coupler schemes [3], pulse pair coherent detection [4], dual-pulse heterodyne methods [5], phase-generated carrier (PGC) [6], coherent phase diversity detection [7], and single-channel detection [8]. These approaches typically integrate hardware and software to demodulate phase and mitigate high-frequency noise. However, these methods may introduce inaccuracies and increase system cost and complexity due to the additional hardware required. In recent years, the application of heterodyne coherent detection technology in Φ-OTDR has drew widespread attention. It provides a wide array of benefits, including expansive sensing range, superior spatial resolution, and cost-effective budget, along with higher sensitivity and improved SNR [9]. With the continues improvement of high-performance of analog-to-digital converters (ADC) and embedded processor, the adoption of digital signal processing (DSP) strategies for executing functions within sensing systems has become increasingly dominated [10]. After heterodyne detection, digital coherent demodulation technologies [11–15] are often employed to capture Rayleigh backscattering light (RBS) phase changes induced by vibrations without adding extra hardware phase demodulation components. However, these technologies typically involve generating digital orthogonal signals from the original signal, which complicates the computation process [16]. Moreover, to filter out high-frequency components from both the original and digital orthogonal signals, matched

---

* Corresponding authors at: Key Laboratory of Intelligent Optical Sensing and Manipulation, Ministry of Education, Nanjing University, Nanjing 210093, China.
E-mail addresses: zyixin@nju.edu.cn (Y. Zhang), nzou@nju.edu.cn (N. Zou).

https://doi.org/10.1016/j.measurement.2025.118214
Received 19 February 2025; Received in revised form 23 May 2025; Accepted 18 June 2025

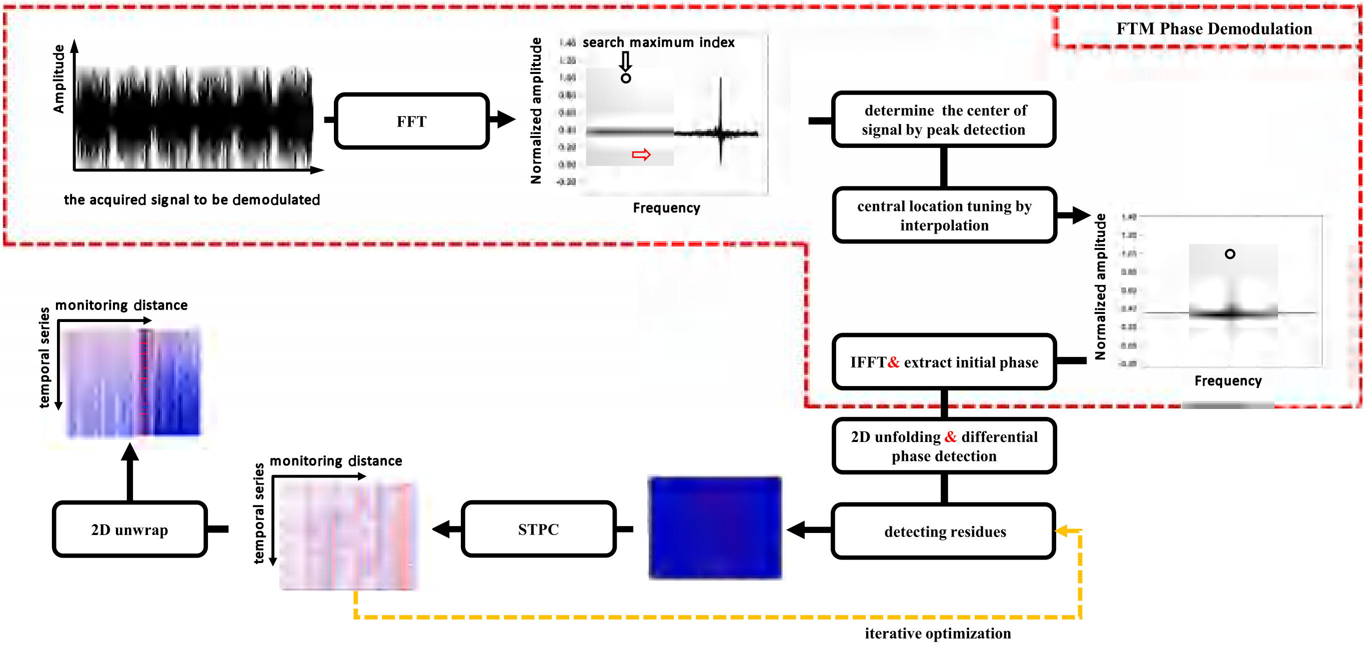

Fig. 1. Overall flowchart of the FTM-STPC.

digital time-domain filters are required. This not only further complicates the computational process but also means that the ultimate demodulation outcome heavily depends on the performance of the digital time-domain filters.

Additionally, the performance of Φ-OTDR systems is significantly weakened by the fading phenomenon [17], where the RBS signals intensity can be severely diminished, submerging it within ambient noise. This phenomenon may lead to significant errors in the demodulated phase leading to either failing to accurately reconstruct true disturbances or misinterpreting false signals as real ones. In response to this limitation, some researchers have proposed system architecture enhancements such as utilizing multiple lasers [18], multiple acoustic-optic modulators (AOMs) [19], adding auxiliary structures [20,21], and integrating multimodal inputs and outputs [22]. These strategies have achieved notable suppression effects. However, improvements in system design typically result in increased equipment costs and complexity. Moreover, for systems already in operation, making structural modifications to reduce fading in the short term may not be feasible. Employing DSP techniques to suppress fading offers a promising approach that does not require modifications to the existing system architecture. A critical aspect of this process involves identifying and mitigating phase fluctuation noise. Currently, the detection of fading points primarily depends on empirical thresholds such as similarity analysis [23,24] or patterns of intensity distribution [25–28]. Although these methods effectively identify the majority of fading regions, they require the adaptation of thresholds for varying situations and cannot precisely identify the fading points within the fading regions. Common approaches to handling identified fading points include their elimination and subsequent infilling [20]. Direct removal of fading points can convert detectable blind spots into permanent dead zones, temporarily compromising the system's detection capabilities. A more advanced method involves leveraging the redundancy and correlations present in the spatiotemporal phase plane to compensate for signals within fading regions [24]. However, when fading points cannot be precisely located, suppressing fading noise through phase compensation always require sacrificing temporal resolution or spatial detail. Currently, some studies have employed deep learning to suppress fading in Φ-OTDR systems [29–32]. These techniques can perform end-to-end fading suppression without prior identification of fading regions. However, they rely on the construction of specific datasets [33], which limits their generalization performance and greatly restricts their adaptability.

In this work, we introduce a novel digital phase demodulation algorithm for heterodyne Φ-OTDR systems that incorporates fading noise suppression without requiring additional phase demodulation or noise suppression modules within the system. This algorithm processes the acquired digital intermediate frequency signals directly, simplifying the system architecture while maintaining effective demodulation performance. In order to address the limitations of using time-domain filters in the digital phase demodulation algorithms, we introduced the Fourier transform method (FTM) [34] which converts the phase demodulation process to frequency-domain processing to achieve adaptive fast filtering, improving speed, accuracy, and SNR compared to traditional I/Q phase demodulation. By introducing residues detection [35], we have achieved precisely identification of the fading points and proposed STPC for lossless phase compensation to suppress fading noise.

2. Principle

Fig. 1 illustrates the FTM-STPC flowchart, utilizing a one-dimensional (1D) optical fiber Rayleigh scattering model for signal demodulation. Initially, the signal is Fourier transformed into the frequency domain, where either the positive or negative frequency components are selectively filtered. Peak detection follows, pinpointing the peak frequency which is then shifted to baseband. Applying the Inverse Fourier Transform extracts the cumulative wrapped phase along the fiber. This phase is subsequently expanded into two dimensions, reflecting the fiber under test (FUT) length, to facilitate differential phase detection for extracting the vibration-wrapped phase. Residue detection is applied to this phase, employing STPC based on the quantitative data from the residue map. This process iterates multiple times until the reduction in the number of fading points in the residue map ceases. Finally, unwrapping yields the vibration phase information free from fading effects. The principles of the algorithm will be specifically described below.

2.1. Phase demodulation based on Fourier transform method

In the heterodyne Φ-OTDR system, the continuous laser emitted at a

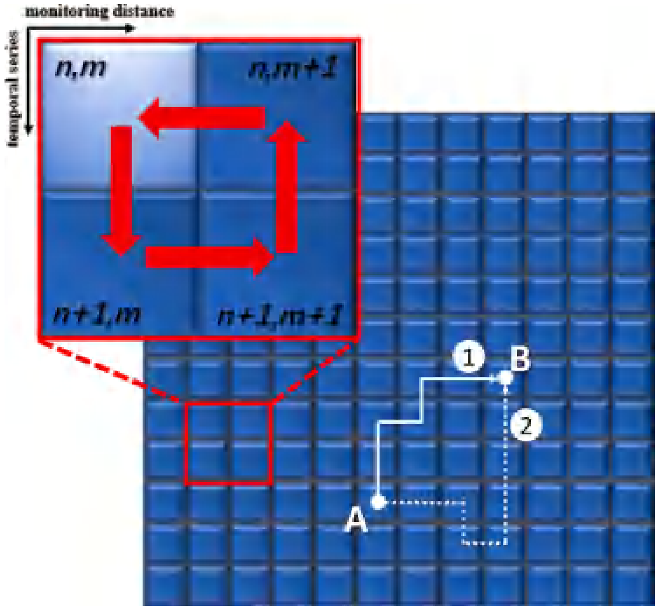

Fig. 2. Path selection and residue detection.

frequency f_{lo} is modulated into pulsed light by a modulator. The frequency of the generated pulsed light is shifted relative to the laser source frequency, and the frequency of the pulsed light would be f_s. The resulting Intermediate Frequency (IF) component current is expressed as

$$I_{IF}(t) = C|E_s||E_{lo}|\cos[2\pi(f_s - f_{lo})t + \varphi(t)] \tag{1}$$

where C denotes the proportionality constant of photoelectric conversion. $|E_s|$ and $|E_{lo}|$ represent the amplitudes of the probe light and the local oscillator light, respectively. The demodulation of the phase term $\varphi(t)$ is achieved through FTM which as illustrated within the red dashed box in Fig. 1. Here, set $b(t) = 1/2C|E_s||E_{lo}|\exp[j\varphi(t)]$. Based on Euler formula, $I_{IF}(t)$ can be re-expressed as

$$\begin{aligned} I_{IF}(t) &= b(t)\exp[-j2\pi(f_s - f_{lo})t] \\ &\quad + b^{*}(t)\exp[j2\pi(f_s - f_{lo})t] \end{aligned} \tag{2}$$

Ignoring frequency drift of the light source, Eq.(2) undergoes a Fourier transform, and applying the Fourier frequency shift property yields

$$F[I_{IF}(t)] = B(-f_s + f_{lo}) + B^{*}(f_s - f_{lo}) \tag{3}$$

where $F[.]$ denotes the Fourier transform operation. $B(.)$ represents the frequency domain distribution of $b(t)\exp[-j2\pi(f_s\text{-}f_{lo})t]$. $B(-f_s + f_{lo})$ and $B^*(f_s\text{-}f_{lo})$ are complex conjugates. As long as $f_s \neq f_{lo}$, B and B^* can be separated in the frequency domain. Centering at the origin and dividing the frequency domain into two regions, $B(-f_s + f_{lo})$ can be effectively extracted. Subsequently, by shifting the frequency point at the maximum value of $B(-f_s + f_{lo})$ to the origin to achieve adaptive frequency shift and eliminate the exponential term $\exp[-j2\pi(f_s\text{-}f_{lo})t]$. This process can be represented as follows

$$b(t) = F^{-1}[F[I_{IF}(t)]\mathrm{G}]\cdot\exp[j2\pi(f_s - f_{lo})t] \tag{4}$$

where $F^{1}[.]$ denotes the inverse Fourier transform operation. G denotes extracting negative frequency component signal. The exponential term $\exp[j2\pi(f_s\text{-}f_{lo})t]$ represents the removal of the $\exp[-j2\pi(f_s\text{-}f_{lo})t]$ by frequency shift. Through this procedure, the phase term $\varphi(t)$ is derived as

$$\varphi(t) = \arctan\frac{imag[b(t)]}{real[b(t)]} \tag{5}$$

2.2. Phase unwrapping and detection of residues

Through the FTM, we can accurately obtain the initial 2D phase distribution in spatial–temporal. However, like other phase demodulation methods, the true continuous phase of the measurement cannot be directly obtained due to the arctangent function for phase calculation, which confines the phase value within the range [-π,π]. For the phase obtained by the Φ-OTDR system, assuming the number of spatiotemporal data points is N and M, respectively. The wrapped phase value in two dimensions and the corresponding true continuous phase value are denoted as $g(n,m)$ and $\varphi(n,m)$, respectively. (n,m) denotes the subscript of the phase map, satisfying $1 \leq n \leq N$ and $1 \leq m \leq M$. The unwrapped phase can be represented as

$$\varphi(n,m) = g(n,m) + 2k(n,m)\pi \tag{6}$$

where $k(n,m)$ takes the value of an integer, forming discontinuous platforms in the 2D space known as truncation platforms. To perform phase unwrapping [33], it is necessary to compare the adjacent wrapped phases to identify the truncation platform. Unwrapping is then carried out along different paths in the truncated 2D wrapped phase, and the first-order derivative is computed in various unwrapping directions. If the difference exceeds π, 2π is added to the phase of the subsequent point; if the difference is less than −π, 2π is subtracted from the phase of the subsequent point. However, obtaining the correct solution is conditional. For example, in Fig. 2, the phases at points A and B are determined, and regardless of whether the unwrapping is performed along path ① or path ②, the result should be the same, i.e., completing a closed loop summation along any path must equal zero. According to the Green theorem, let the closed region D be bounded by a piecewise smooth curve L. If the functions X and Y are continuous on the closed region D and possess continuous first-order partial derivatives, then

$$\iint_D [\frac{\partial X}{\partial x} - \frac{\partial Y}{\partial y}]dxdy = \oint_L Xdx + Ydy \tag{7}$$

The equivalent conditions for the path integral being independent of the choice of path is that

$$\oint_L Xdx + Ydy = 0 \quad or \quad \frac{\partial X}{\partial x} - \frac{\partial Y}{\partial y} = 0 \tag{8}$$

The first-order derivatives of the 2D wrapped phase with respect t to the spatial direction and the temporal direction are denoted as X and Y, respectively.

$$X = \frac{\partial g}{\partial x} = \Delta g^{x}, \quad Y = \frac{\partial g}{\partial y} = \Delta g^{y} \tag{9}$$

The phase unwrapping from A to B along path ① in space is equivalent to

$$\int_{①} Xdx + Ydy \tag{10}$$

The condition for the phase unwrapping to be independent of the chosen path is $\partial X/\partial x\text{-}\partial Y/\partial y = 0$ [36]. During demodulation of the Φ-OTDR system signals, the fading points must not satisfy this condition when the Nyquist sampling is satisfied, and points that do not meet this condition are typically referred to as residues [35].

After unwrapping, these residues always cause the propagation of unwrapping errors. Therefore, the location of fading points can be determined by conducting residues searches on the initial phase map. Herein, we provide a comprehensive description of the methodology for detecting residues. Specifically, the phase difference loop integration is performed on the theoretically smallest closed loop path, namely the 2 × 2 cell closed loop, to mark the corresponding non-zero regions. For the point (n, m) located within the 2 × 2 cell closed loop delimited by the red box in the upper-left corner of Fig. 2. If Δ_{ij} (ij = 00, 01, 10, 11)

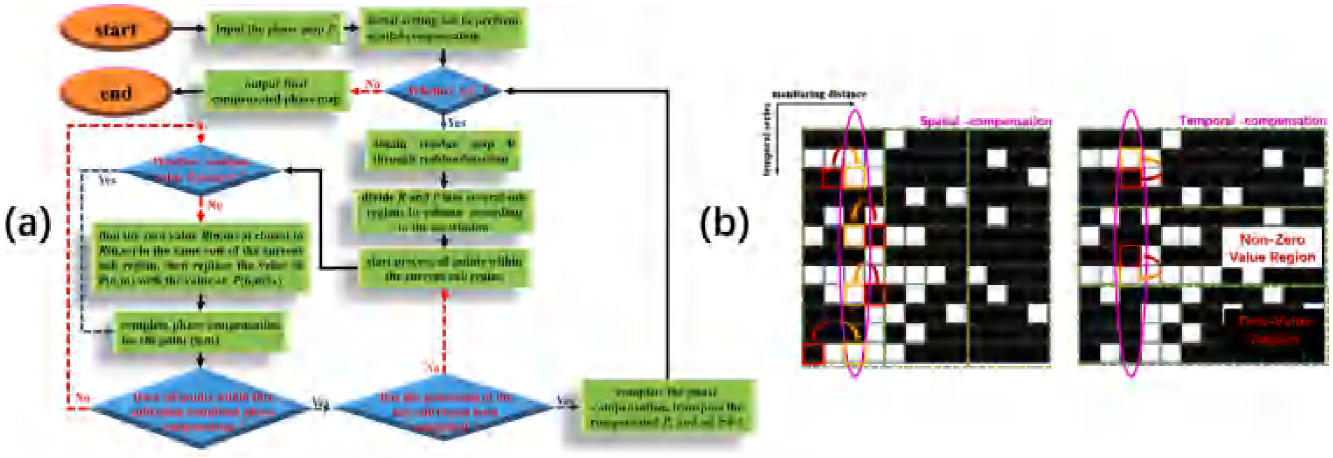

Fig. 3. (a) STPC algorithm flowchart; (b) Schematic diagram of fading noise suppression based on STPC.

represents the phase difference between adjacent points, the first-order derivative is computed as

$$\begin{cases} \Delta_{00} = g(n+1,m) - g(n,m) \\ \Delta_{01} = g(n+1,m+1) - g(n+1,m) \\ \Delta_{10} = g(n,m+1) - g(n+1,m+1) \\ \Delta_{11} = g(n,m) - g(n,m+1) \end{cases} \tag{11}$$

where g(n + 1, m) − g(n, m) is the discrete form of the partial differential of the phase in the time direction at point (n, m). Using this point as the origin, the cumulative wrapped phase differences along the 2 × 2 pixel closed-loop path are summed to calculate

$$R(n,m) = \sum_{i=0}^{1}\sum_{j=0}^{1}\Delta ij = \frac{\partial Y}{\partial y} - \frac{\partial X}{\partial x} \\ = W\{\Delta_{00}\} + W\{\Delta_{01}\} + W\{\Delta_{10}\} + W\{\Delta_{11}\} \tag{12}$$

where $W\{.\}$ denotes the wrapping operator, which constrains the phase to its principal value within the range $[-\pi,\pi)$. $R(n,m)$ corresponds to the closed-loop integral over a 2 × 2 pixel neighborhood. If $R(n,m) = 2\pi$, the point is identified as a positive residue. Conversely, a value of $R(n,m) = -2\pi$ indicates a negative residue. In our work, the corresponding 2 × 2 cell closed loop is marked as a residue, and all these residue values are expressed as 1.0. When $R(n,m) = 0$, then the point is not a residue.

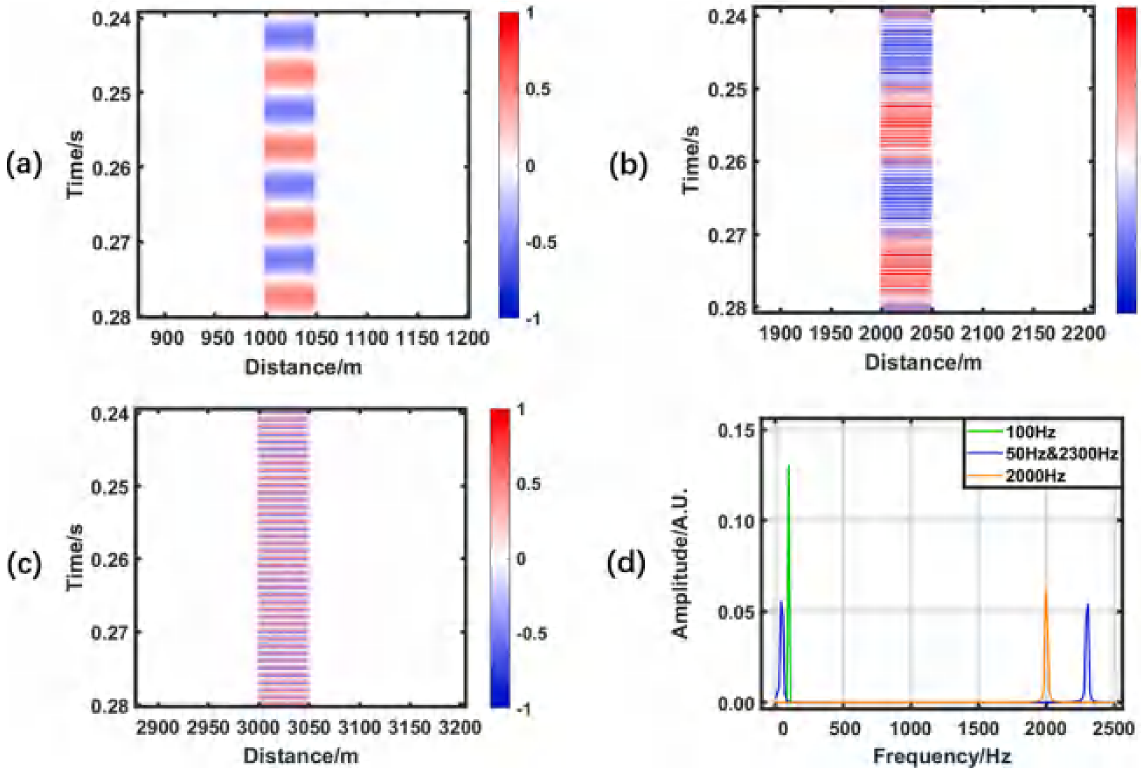

Fig. 4. Phase demodulation results of numerical model based on FTM. (a)waterfall plots of vibration at 100 Hz; (b) waterfall plots of vibration at the combination of 50 Hz with 2300 Hz; (c)waterfall plots of vibration at 2000 Hz; (d)frequency spectrum of the vibration center signal.

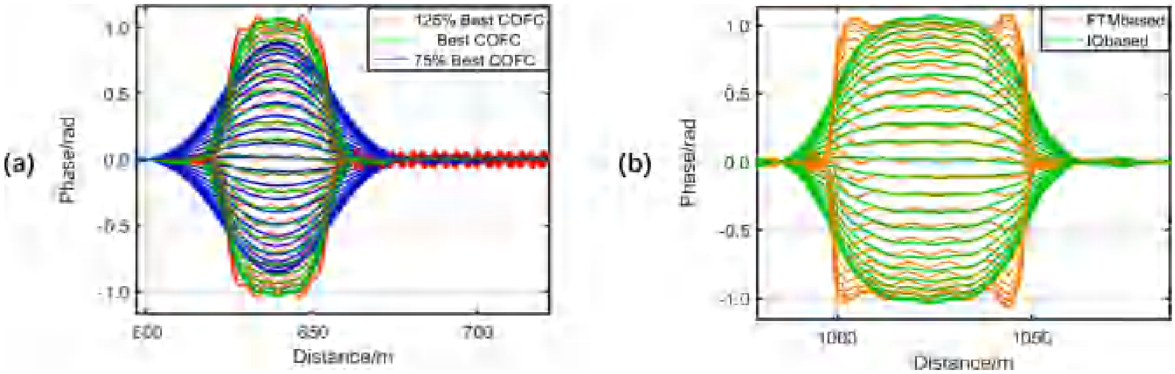

Fig. 5. (a) I/Q phase demodulation results at different filtering bandwidths; (b) phase spatial distribution of vibration signals demodulated by FTM and I/Q at different times.

2.3. Quantification and suppression of fading noise

Phase compensation can be performed based on the distribution of residues. In order to achieve quantitative characterization of the residues. In this work, we design an operator to characterize the value with the maximum proportion of non-zero values among all sliding windows in the residue map, namely the maximum non-zero element proportion (NZP_{max})

$$NZP_{\max} = \max_{S \in \{1, 1+step, \dots, M\}} \left\{ \frac{\sum_{n=1}^{N} \sum_{m=S}^{S+\omega-1} 1[R(n,m) = 1]}{Nw} \right\} \tag{13}$$

where the sliding window w is set to the interval of the differential phase detection mentioned in Fig. 1, and step size set to $step = w/2$. This function quantitatively characterizes the variation of fading points by computing the proportion of non-zero elements within each sliding window of the residue map and identifying the window with the maximum non-zero element proportion. The function has a maximum value of 1 and a minimum value of 0, with larger values indicating a higher density of fading points in the region.

The following step will be to suppress fading by the phase compensation algorithm STPC. STPC can be divided into spatial and temporal parts. This process involves partitioning the data into multiple subregions based on the width of the differential phase detection interval w in the spatial domain and temporal domain. Leveraging the redundancy and local correlations of the phase map [28] to replace phase value corresponding to the non-zero indices in the residue map within these sub-regions. As shown in Fig. 3(a), the compensation procedure first searches for the nearest zero-value region in the spatial dimension; if none is found, a similar search is conducted in the temporal dimension to locate the zero-value phase points for replacement. As shown in Fig. 3 (b), the figure specifically illustrates the phase compensation process in the third column.

3. Simulation analysis

3.1. Phase demodulation results of FTM

To quantitatively assess and analyze the performance of FTM-STPC, we verified and compared the accuracy of phase demodulation and the applicability range of phase compensation using a numerical model. Inspired by [37], we conducted a comparative analysis using simulated signals generated by a simplified numerical model. In the Section A, in order to accurately quantify the performance of different phase demodulation algorithms, no noise was added to the numerical model. FUT was set to 4 km to cover a typical range of practical applications and provide sufficient data to assess system performance. To simulate disturbances at different positions and frequencies, sinusoidal testing signals with an amplitude of ±0.5 rad covering a span of 50 m were applied at fiber positions of 1000 m, 2000 m, and 3000 m. The frequencies of these sinusoidal test signals were set to 100 Hz, and a combination of 50 Hz with 2300 Hz and 2000 Hz, respectively. The pulse repetition frequency was set to 5 kHz and the spatial resolution of the system was 1 m. Fig. 4 shows the corresponding phase demodulation results based on FTM.

These results demonstrate the capability of the FTM algorithm to accurately demodulate the phase to obtain the corresponding precise position information and frequency information of vibration signal.

Furthermore, we compared the performance between FTM and the representative I/Q phase demodulation algorithm. Fig. 5(a) depicts the phase demodulation results of two digital time-domain low-pass filters used in I/Q phase demodulation with different filtering bandwidths, where each result corresponds to 100 time-continuous phase curves. The figure illustrates when the filtering bandwidth is set to 125 % of the bandwidth of the matched filter (BoMF), the I/Q demodulation process amplifies high-frequency components inherent to the transient features of signal, creating artifacts that mimic noise. Conversely, reducing the filtering bandwidth to 75 % of the BoMF can suppress these artifacts but degrade accuracy by smoothing critical signal details. Therefore, it is crucial to balance the filtering bandwidth of the low-pass filters to achieve an optimal trade-off between retaining the signal quality and minimizing noise, ensuring both accurate phase information and noise reduction. In contrast, FTM uses adaptive frequency-domain filtering to remove corresponding components with conjugate terms, accurately demodulating the respective RBS phase signals without introducing filter-induced artifacts. As shown in Fig. 5(b), compared to the I/Q phase demodulation using the bandwidth of the matched filter, the phase curve at any given time point can accurately determine the spatial distribution of the vibration signal by the FTM phase demodulation. Due to the suppressive effect of the digital time-domain filter, the results of digital I/Q phase demodulation exhibit a smoother spatial distribution. However, this smoothing effect also introduces phase errors. We extracted the time-domain vibration waveform at the vibration center location (1025 m) and presented the phase demodulation results under different phase disturbance amplitudes in Fig. 6. The results demonstrate that FTM can accurately demodulate the phase with high precision across a range of disturbance amplitudes. In contrast, when the phase disturbance amplitude is smaller, the digital time-domain filter has a more significant impact on the I/Q demodulation, leading to increased phase demodulation errors, and the baseline fluctuations caused by filter-induced artifacts is significantly higher than that of FTM. At the position of 3000 m with phase disturbance frequency of 500 Hz, it can be observed that despite the phase disturbance reaching ±5.0 rad, this combination of frequency and amplitude ensures that the phase difference between adjacent points does not exceed π, thus preventing errors during the phase unwrapping process. However, the demodulation results from I/Q demodulation already show significant distortion,

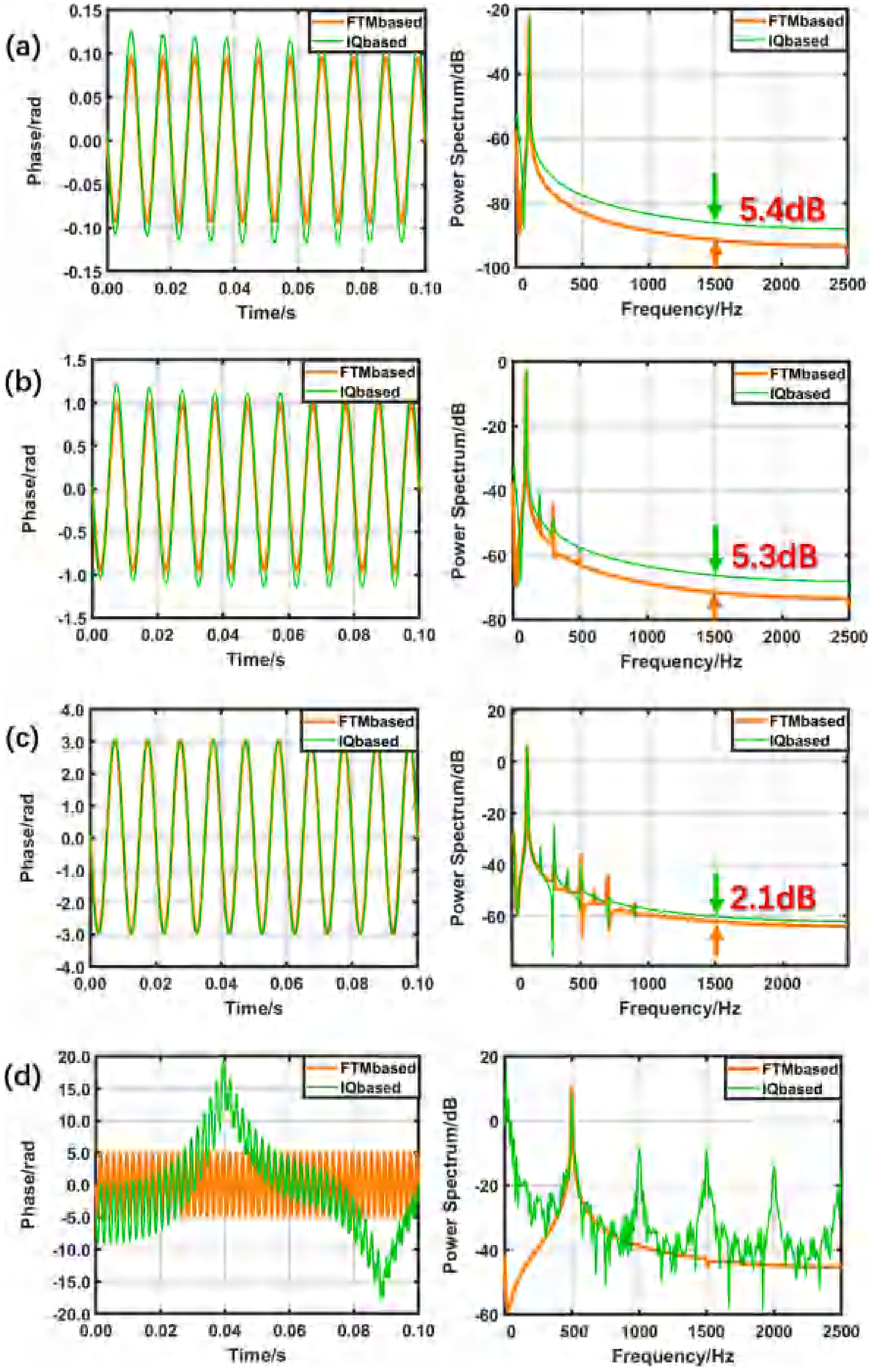

Fig. 6. The demodulation results of different phase disturbance amplitudes, where (a) to (d) are the Temporal waveform plots (left) and PSD plots (right) under different phase disturbance amplitudes. (a) disturbance amplitude of ±0.1 rad; (b)disturbance amplitude of ±1.0 rad; (c) disturbance amplitude of ±3.0 rad; (d) disturbance amplitude of ±5.0 rad; (e) spatial–temporal waterfall of partial different demodulation results and polygon-fitted histogram of SNR and SSIM for 1000 sets of different demodulation results.

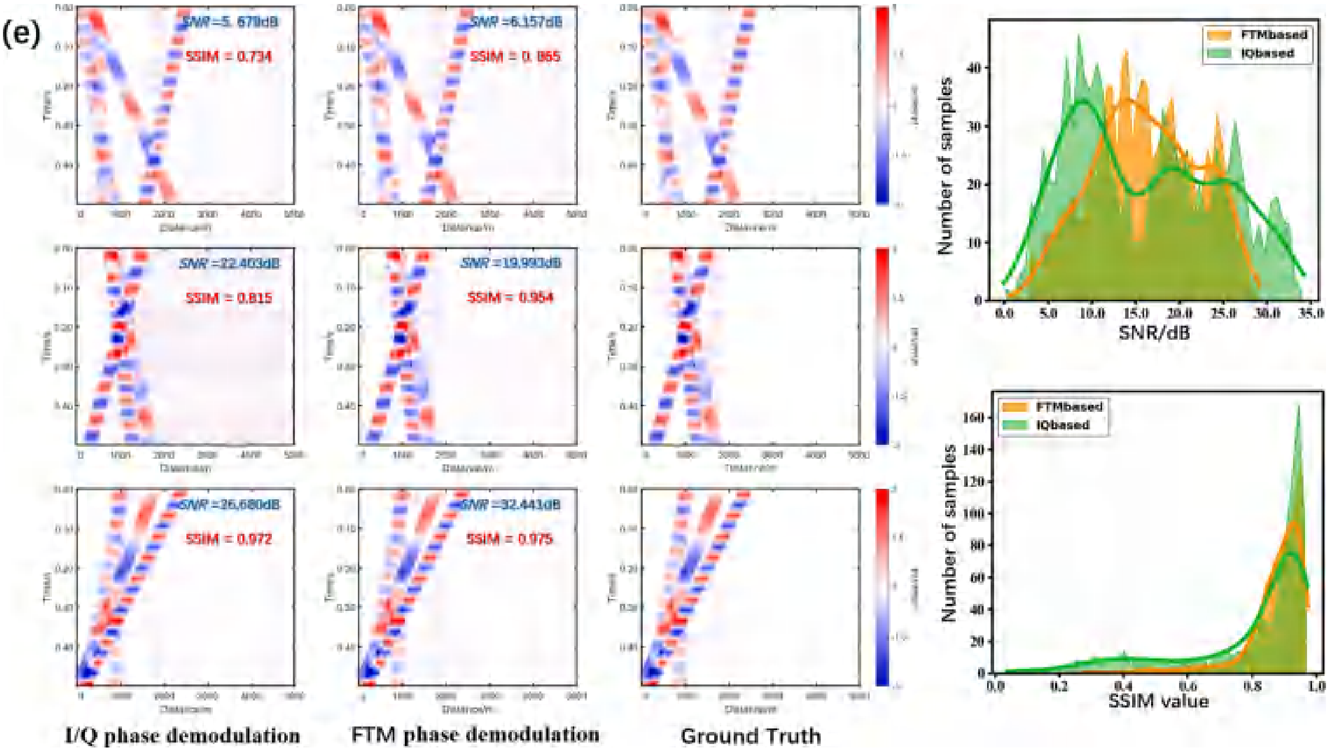

Fig. 6. (*continued*).

whereas FTM continues to accurately demodulate the corresponding phase values, demonstrating a stronger anti-interference capability. To demonstrate the advantages of the FTM algorithm, we randomly applied up to 20 perturbation signals across a 5 km range, with each disturbance amplitude of signal set to $\pm x$ rad, where x ranges from 0 to 3. Additionally, to increase the complexity and realism of the test, we randomly set the initial phase difference between the probe light and the local oscillator light, and generated IF signals with randomly varying center frequencies. We generated 1000 datasets and displayed three sets of demodulation results in Fig. 6(e), the series of spatio-temporal waterfall plots display the performance metrics for different testing conditions across several frequencies and disturbances. This research computed the SNR and Structural Similarity Index Measure (SSIM) [38] for the demodulation results from both the FTM and digital I/Q demodulation by comparing them against the Ground Truth. SNR was used to assess the noise resistance of the algorithms, while SSIM, which ranges from 0 to 1, with values closer to 1 indicating higher similarity, was used to evaluate the accuracy of demodulation. On the far right of the Fig. 6(e), the polygon-fitted histograms effectively summarize the SNR and SSIM outcomes. These histograms, shown in green and orange, demonstrate the variance and distribution of SNR and SSIM values across 1,000 demodulation tests. The SNR histogram reveals that the FTM algorithm predominantly exhibits higher peaks and a denser distribution in the moderate to high SNR range (10 to 30 dB), suggesting that the FTM algorithm introduces less phase noise during the demodulation process and has stronger noise resistance. Moreover, the SSIM histogram indicates that samples from the FTM algorithm are predominantly concentrated around the maximum value of 1, with few samples falling below 0.5. This highlights its superior ability to maintain accurate demodulation. In contrast, the digital I/Q demodulation exhibits a significantly lower number of samples in the high SSIM range. Although there is a reasonable number of samples within the 0.6 to 0.8 interval, the performance near SSIM value 1 is poor, and a portion of the samples falls below 0.5, indicating a higher probability of demodulation failure. This further demonstrates that under the same conditions, the demodulation accuracy of the digital I/Q modulation is inferior to that of the FTM algorithm. In this work, both FTM and I/Q demodulation were computed on an X86 computer equipped with an AMD Ryzen 7 5800H CPU operating at 3.20 GHz and 64 GB RAM, processing the same simulated dataset ($N \times M = 2500 \times 5000$). The computational time for I/Q demodulation is 0.893 s per data, while FTM takes only 0.491 s per data. These times represent the average computational times over 1000 sets of data.

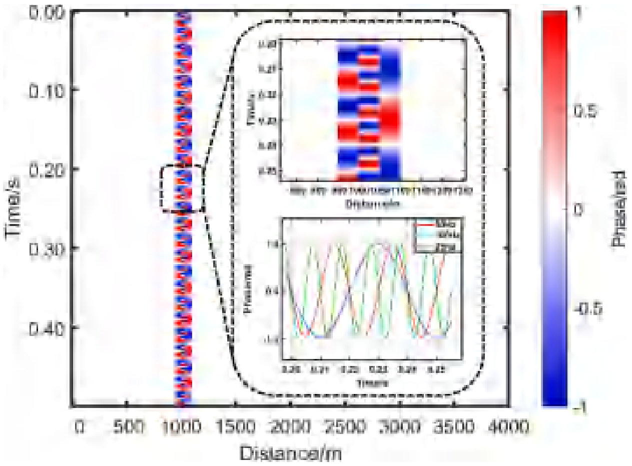

Fig. 7. Phase distribution of numerical model with closely spaced disturbances at three different vibration frequencies and disturbance amplitude of ±1.0 rad.

3.2. *Fading suppression results of STPC*

We further investigate the performance of STPC for fading noise suppression. To demonstrate that phase compensation does not cause spatial distribution distortion, the numerical model was used where sinusoidal interference signals with frequencies of 50 Hz, 100 Hz, and 25 Hz are applied at 950 m, 1000 m, and 1050 m of the FUT, respectively.

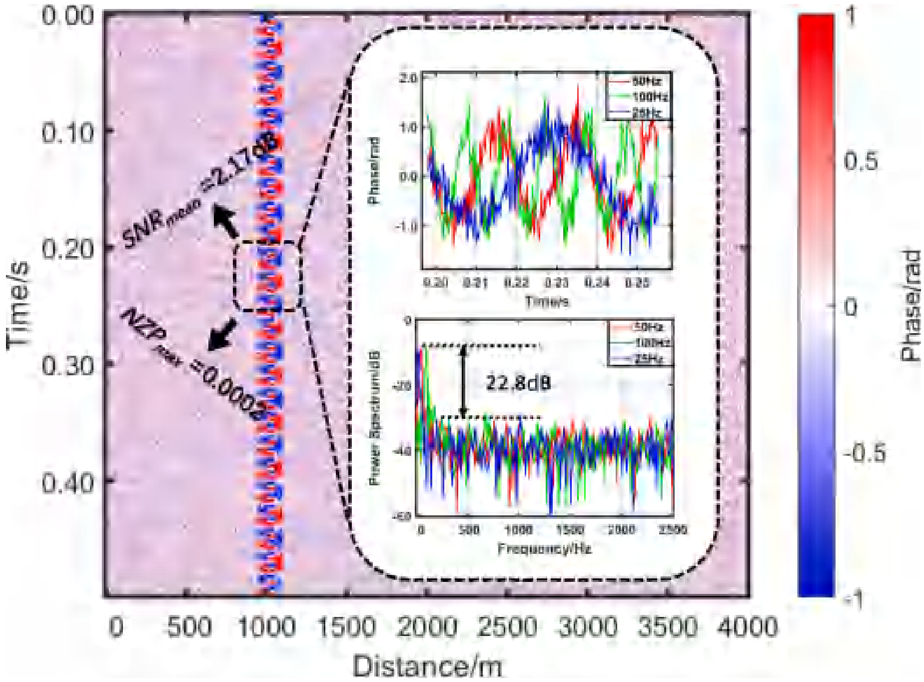

Fig. 8. Phase demodulation result of numerical model with only Gaussian white noise.

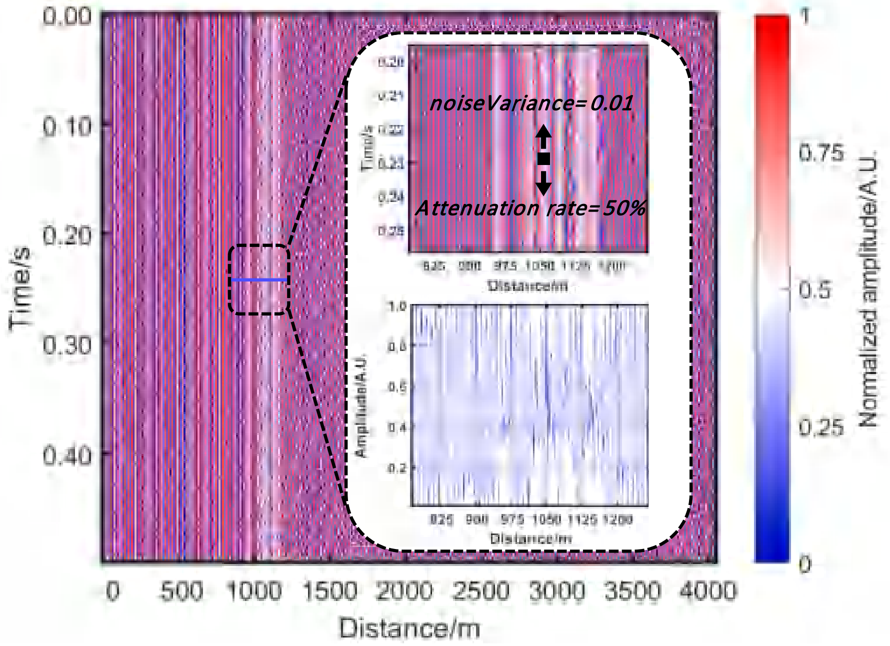

Fig. 9. Beat signals of numerical model with variance of 0.01 and signal amplitude attenuation of 50% in partial regions.

Each vibration signal has a length of 50 m, and all phase disturbance amplitudes were set to ±1.0 rad. Other parameter settings are consistent with Section A. Fig. 7 presents the phase distribution, where the three vibrational signals are closely connected. This signal distribution setup ensures that the results obtained when validating the phase compensation of STPC for vibration events occurring within fading regions are sufficiently reliable. Within fading regions, the intensity of the beat signal significantly decreases and can become submerged in environmental noise which follows a normal distribution [36]. To enable systematic analysis of algorithm robustness under controllable conditions, we intentionally decoupled the attenuation magnitude (deterministic parameter) and noise intensity (probabilistic parameter) in our simulations. This design choice prioritizes parametric interpretability over physical noise-generation mechanisms. Specifically, we simulated fading noise by attenuating the beat signal and added Gaussian white noise. To achieve quantitatively controlled fading noise generation, a single fading region is implemented through the following steps. First, the peak-finding algorithm is used to identify the index positions of the maximum and minimum peaks of the normalized beat signal. Then, an arbitrary maximum peak index is chosen as the starting point, and the

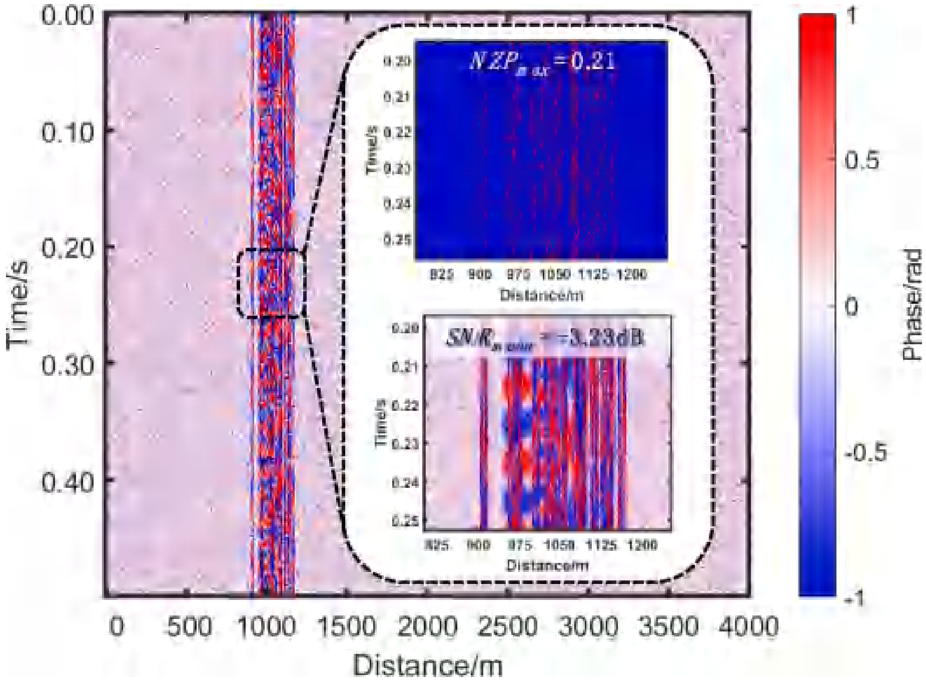

Fig. 10. Phase demodulation result of numerical model with fading noise but without fading noise suppression.

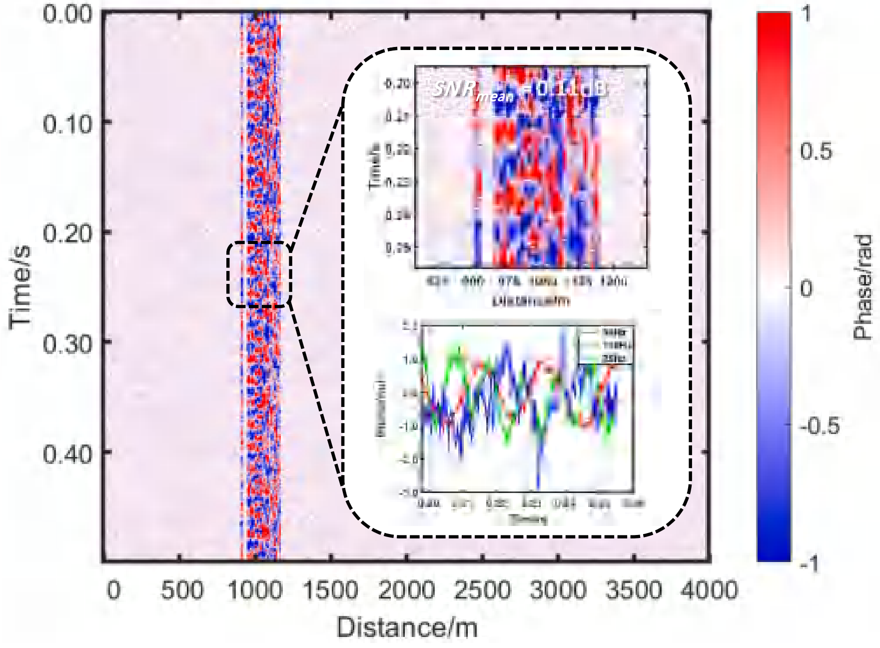

Fig. 11. Phase demodulation result of numerical model with OWA fading noise suppression.

subsequent even-numbered minimum peak indices are selected as the endpoints. Finally, the amplitude of the beat signal within a region is attenuated by a random coefficient. Additionally, the added Gaussian white noise is controlled by tuning the Gaussian distribution variance of the noise. For reference, we initially apply Gaussian white noise with a variance coefficient of 0.01 to the all regions without attenuating the beat signal. The corresponding demodulation results, as shown in Fig. 8, indicate that for this segment of the signal, with a correlation coefficient $NZP_{max} = 0.0002$, the signal remains unaffected by fading noise. Here, we evaluate the overall quality of the signal in this region by calculating the average SNR of each column (SNR_{mean}). Further, to explore the effects of fading, random attenuation is applied to the beat signal in the region where the vibration signal is located, as illustrated in Fig. 9. Specifically, within this 200 m interval, random regions are selected, and each region was attenuated by 50 % on their intensity. This approach of fixing the attenuation levels is primarily adopted to simplify subsequent discussions regarding the impact of different variance levels on the results. The corresponding FTM demodulation results are shown in Fig. 10. The residue map reveals that within the designated fading regions, the beat signal, submerged in Gaussian white noise, results in

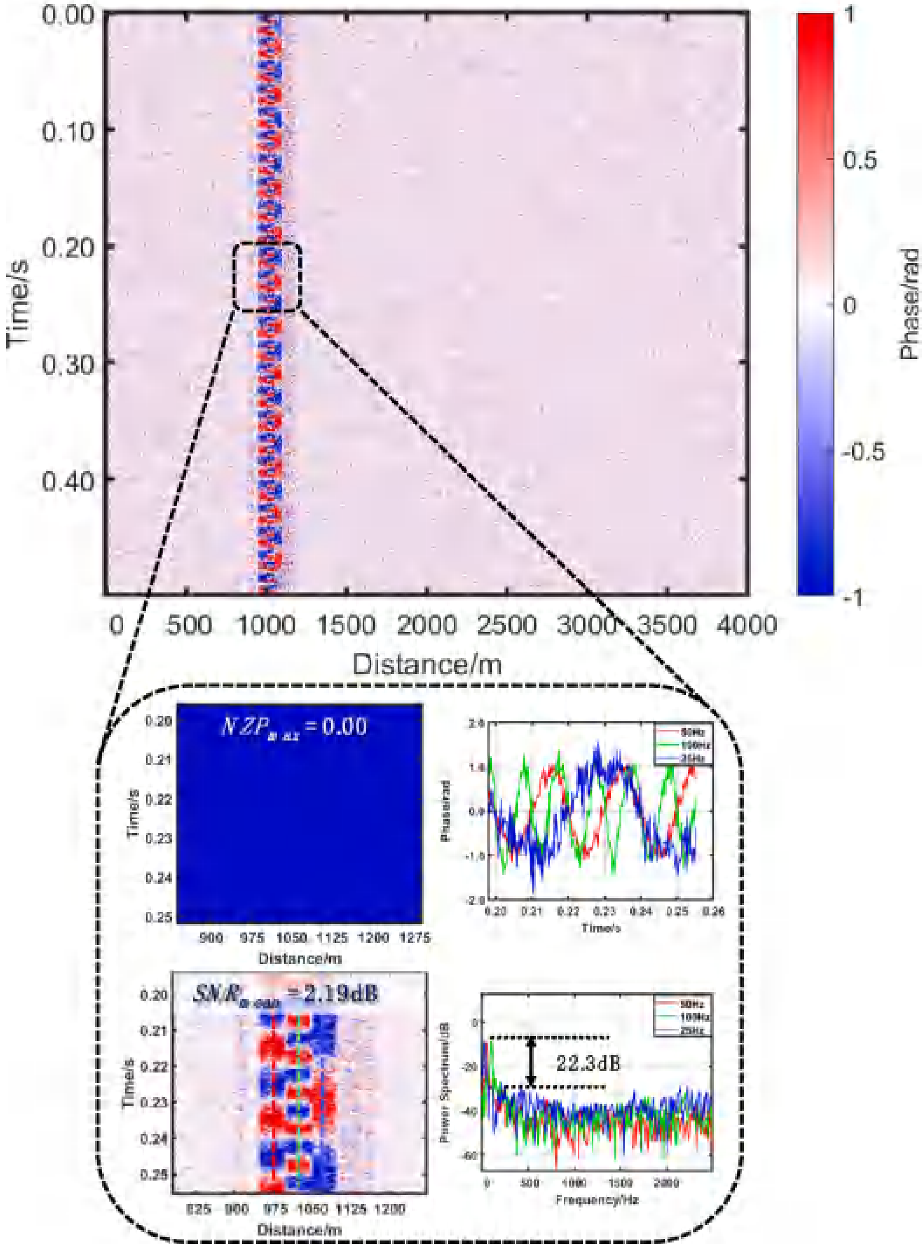

Fig. 12. Phase demodulation result of numerical model with STPC fading noise suppression.

non-zero values, identified as fading noise spots. This condition leads to complete distortion of the vibrational signals that fall within these fading regions. For comparative purposes, we initially employed the optimal weighted average algorithm (OWA) [25] to mitigate fading noise. However, as illustrated in Fig. 11, this algorithm exhibits limitations when dealing with signals in extensive fading regions. This may result in distortion of vibration signals and cannot quantitative assessment of fading noise suppression, relying solely on imprecise comparisons through changes in SNR_{mean} within the respective region. Particularly noteworthy is the lack of reference data required to compute SNR_{mean} when utilizing real experimental data, thereby impeding accurate measurement of the algorithm compensatory effects. The outcomes of STPC are illustrated in Fig. 12. It can be observed that, following phase compensation, where $NZP_{max} = 0$, the vibration signals within the region are no longer influenced by fading noise. Spatial-temporal waterfall plots show that no overlap or difference between the positions corresponding to the different frequencies after compensation.

In practical scenarios, different components in Φ-OTDR systems can lead to varying levels of noise floor. To further explore the generalization of the STPC algorithm, we investigated the impact of different noise floor levels under fixed attenuation conditions. We changed the variance in the fading regions, starting from 0.001, with the corresponding beat signals displayed in Fig. 13 depict the demodulation results of the FTM without phase compensation and the FTM-STPC with compensation, respectively. It is observed that even at extremely low noise levels (the Gaussian distribution of noise has a variance of 0.001), despite significant attenuation of the beat signal, there is no substantial generation of fading noise. This indicates that the appearance of fading noise is correlated not only with the attenuation of the beat signal but also with the ambient noise burying it. Consequently, determining fading regions merely based on the intensity threshold of the beat signal is inaccurate. As the noise within the region increases, even though fading points irregularly emerge, STPC still manages to accurately restore the vibrational signal to some extent. The decline in demodulation accuracy is primarily due to the large-scale random phase noise caused by the

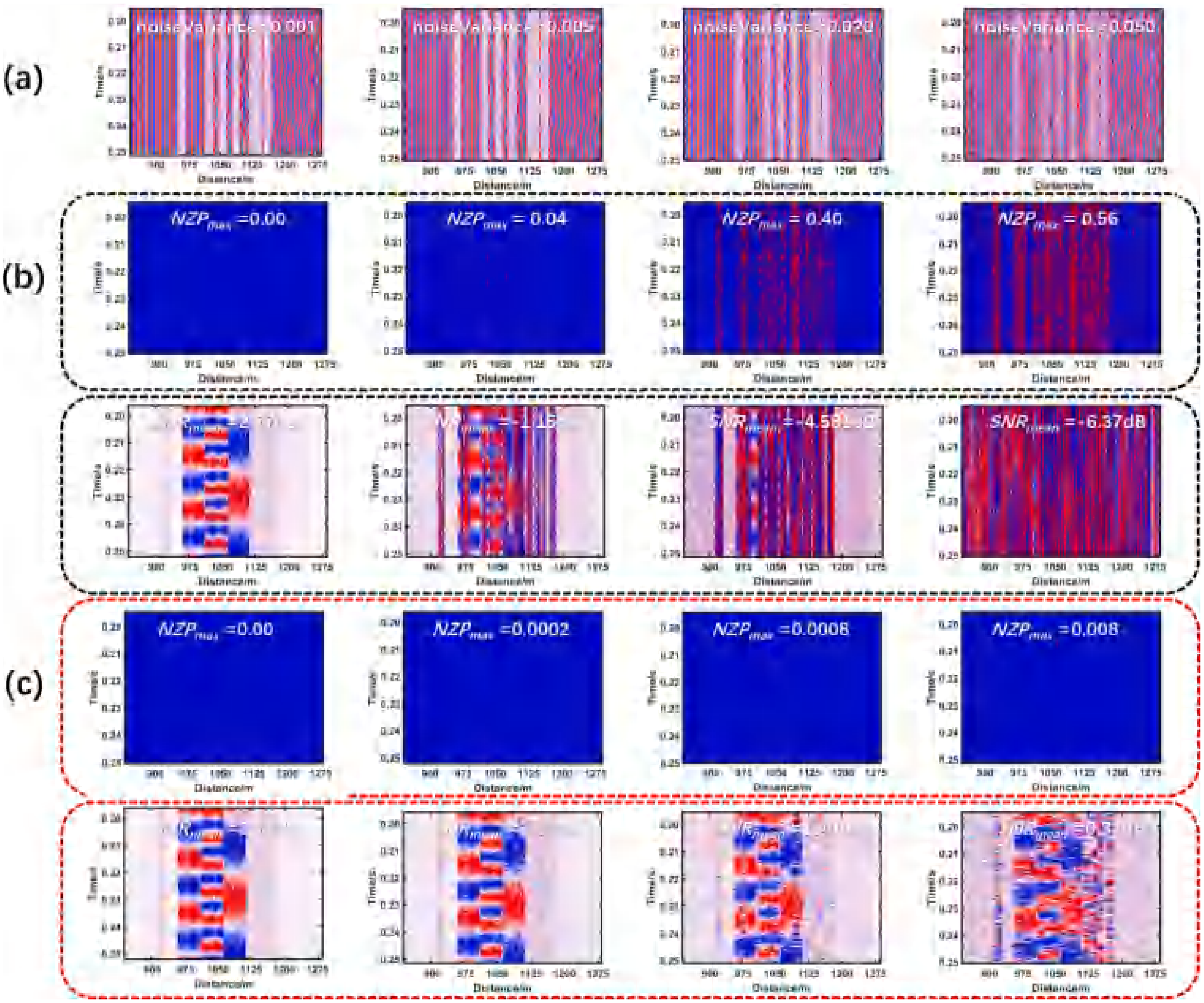

Fig. 13. Phase demodulation results of simulation model for FTM-STPC suppression of fading noise when different noise variance is applied. (a) Beat signals with different noise variances; (b) FTM demodulation results with different noise variances; (c) FTM-STPC results with different noise variances.

applied Gaussian white noise, which destroys the original phase signal.

4. Experimental results

Based on the analysis of the simulation results, we believe these findings offer valuable insights for practical applications. To validate the effectiveness and feasibility of the simulation results, we further evaluate the overall performace of FTM-STPC through experiments. The experiment in this work based on a standard heterodyne Φ-OTDR system [37]. As illustrated in Fig. 14, the system utilizes a high-coherence narrow linewidth laser (NLL) with a wavelength of 1550 nm as the light source. The continuous light emitted from the NLL is divided by Optical Coupler 1 (OC1) into two streams: 90 % as probe light and 10 % as local oscillator light. The probe light is modulated by an AOM into light pulses lasting 50 ns with an 80 MHz frequency shift and amplified through an erbium doped fiber amplifier (EDFA) with a current value set to 65 mA. Subsequently, the amplified light pulses are directed into the sensing fiber via a circulator, and part of this fiber is wrapped around a piezoelectric transducer (PZT) to simulate external disturbances using the vibrations of the PZT. Within the sensing fiber, the RBS interferes with the local oscillator light in Optical Coupler 2 (OC2), creating a beat signal that is detected by a BPD and recorded by a data acquisition card (DAQ). The triggering pulses are provided by a pulse generator (PG), pulse repetition frequency is set to 20 kHz. The probe pulse is injected into the 2.5 km FUT, with approximately 50 m FUT wound around a PZT located at a distance of 2040 m. Subsequently, a sinusoidal wave of 1 V and 100 Hz was applied to the PZT and the sampling time is 0.5 s. As shown in Fig. 15(a), the actual acquired beat signals show varying degrees of spatial attenuation. Fig. 15(b) and (c) present the spatial–temporal waterfall plots obtained directly through FTM and I/Q demodulation. Without fading noise suppression algorithms, the overall demodulation results are typically affected by fading noise. A comparative analysis of both demodulation algorithms in selected vibration regions reveals that the NZP_{max} coefficient for I/Q demodulation is nearly twice that of FTM, demonstrating FTM's superior noise resistance. Further comparison involved analyzing locations at 2052 m, unaffected by fading noise, and 2062 m, affected by fading noise, as shown in Fig. 15(d) and (e). At the location free from fading noise interference, both FTM and I/Q accurately demodulate the RBS vibration phase signal, displaying good smoothness and periodicity with precise frequency demodulation and no significant harmonic interference in spectral analysis. The spectral intensity of the FTM demodulation results is slightly higher than that of I/Q in the frequency spectrum. At locations affected by fading noise, the demodulation results from

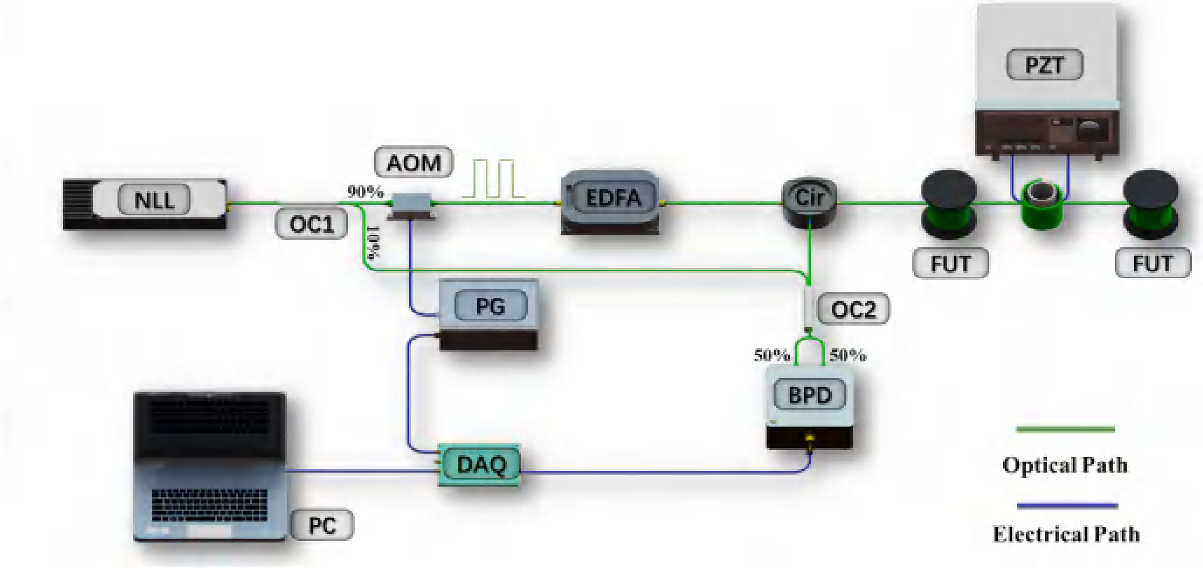

Fig. 14. The schematic diagram of heterodyne Φ-OTDR system.

both FTM and I/Q exhibit significant distortions in the waveform. However, due to its enhanced noise resistance, the FTM still accurately represents the actual peak frequency of 100 Hz in the spectral analysis, whereas the I/Q results are entirely inaccurate.

Next, we further explore the effectiveness of the STPC algorithm through experimental data. As shown in Fig. 16(a), following phase compensation via the STPC algorithm, the NZP_{max} is reduced from an initial value of 0.28 to 0.0002, achieving a fading suppression rate of 99.93 %. Fig. 16(b) illustrates the results before and after the application of the STPC algorithm in the region unaffected by fading noise. The temporal waveform plot, PSD plot, and frequency spectrum overlap completely, indicating that using the STPC algorithm to compensate for fading regions in adjacent phases does not affect regions that are not experiencing fading noise. As depicted in Fig. 16(c), in the regions originally affected by fading noise, the STPC algorithm restores the nearly completely distorted waveforms to accurate representations. The PSD plot and frequency spectrum demonstrate that distortions within the low-frequency range are fully suppressed, with an improvement in SNR of 18.9 dB.

In the previous section, we applied the OWA algorithm in an attempt to suppress fading noise in simulated vibration signals across most areas, but the results were suboptimal. In this section, we apply the OWA algorithm to experimental data, as illustrated in Fig. 17(a). Due to the difficulty in quantitatively assessing the residual fading noise in the processed results using the OWA algorithm, direct observation reveals that, although the fading noise in the vibratory areas has been largely suppressed, significant interference persists in regions that should be non-vibratory but are still affected by fading noise. This outcome is in contrast to the use of the STPC algorithm, depicted in Fig. 16(a), which more effectively mitigated fading noise. Further, we have plotted the spatial phase value curves between 0.275 s and 0.285 s, as illustrated in Fig. 17(b), (c), and (d). Comparing these with the original phase curves without fading suppression, it is clear that both algorithms reveal the locations and amplitudes of vibrations distinctly. However, in terms of spatial detail, such as at the 2120 m mark circled in the diagrams, STPC demonstrates superior spatial resolution. This advantage is attributed to STPC's precise identification and replacement of fading points. In non-vibratory regions, STPC accurately locates and replaces fading points as well, restoring the phase noise caused by fading to a normal, smoother phase value.

To further investigate the reliability and applicability of the FTM-STPC algorithm, we modified some experimental conditions and system parameters. As shown in Fig. 18, we reduced the pulse repetition frequency to 1 kHz and injected the probe pulse into a 3.5 km FUT. Additionally, at the 2.6 km position, approximately 100 m of the FUT were coiled, and this coiled 100 m of FUT was placed under a 3 kg iron plate with a thickness of 5 cm. A 1 kg acrylic cylindrical barrel with a diameter of 15 cm was positioned on the iron plate. Subsequently, a 2.7 g ping-pong ball fell into the barrel from a height of 0.5 m and was bounced up by the iron plate, generating an underdamped vibration signal with gradually decreasing amplitude. In order to explore the different noise environments, we adjusted the current of the EDFA to alter the intensity of the optical pulses and recorded the phase noise gradually increasing corresponding to three data sets with EDFA currents set at 65 mA, 60 mA, and 55 mA, respectively. We analyzed the last second data of each group of underdamped vibration signals. As illustrated in Fig. 19(a), with decreasing EDFA current values, direct demodulation using FTM reveals not only an increase in random phase fluctuations of RBS but also an overall escalation in fading noise. At an EDFA current of 55 mA, the vibration locations nearly completely fall into fading regions. At the 2580 m position, the corresponding temporal waveform plots progress from partial to complete distortion. Fig. 19(b) displays the outcomes after applying STPC, where the NZP_{max} values decreased by approximately three orders of magnitude, and the fading noise suppression rates exceeded 99 %. The waveforms at the 2580 m position were restored, with the corresponding vibration spectral peak frequencies reverting to approximately 43 Hz. When phase noise is not significant, STPC accurately restores the ideal underdamped vibration waveform pattern. Fig. 19(c) provides a more intuitive display of the PSD heatmap for the one second interval from 1900 m to 3200 m. This visualization clearly illustrates the conditions before and after the application of the STPC algorithm. Even under conditions of significant random phase noise, STPC can still compensate and accurately restore the correct vibration signals, consistent with the findings discussed in the previous section using simulated signals to explore varying amplitude SNR in intermediate frequency signals.

5. Discussion

In this work, we introduce a novel digital phase demodulation algorithm for heterodyne Φ-OTDR systems that directly processes intermediate frequency signals, simplifying system architecture and maintaining high demodulation performance without additional modules. In the Φ-OTDR digital phase demodulation segment, we introduce

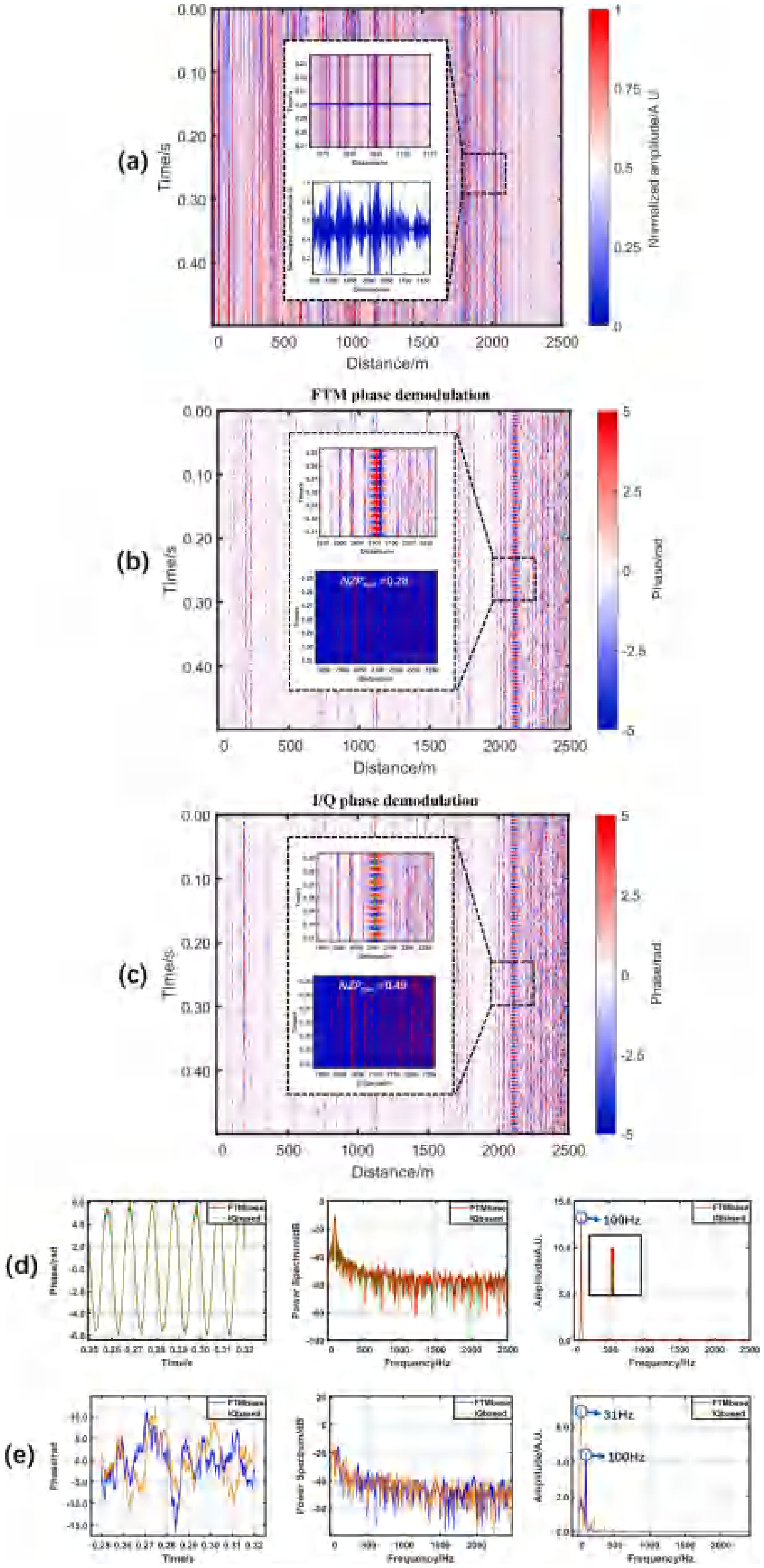

Fig. 15. Demodulation results when 100 Hz sinusoidal vibration is applied. (a) spatial–temporal beat signals; (b) waterfall plot of FTM phase demodulation without fading suppression; (c) waterfall plot of I/Q phase demodulation; (d) from left to right, the sub-plots show the temporal waveform plot, PSD plot, and frequency spectrum of different demodulation algorithms at 2052 m position; (e) from left to right, the sub-plots show the temporal waveform plot, PSD plot, and frequency spectrum of different demodulation algorithms at 2062 m position.

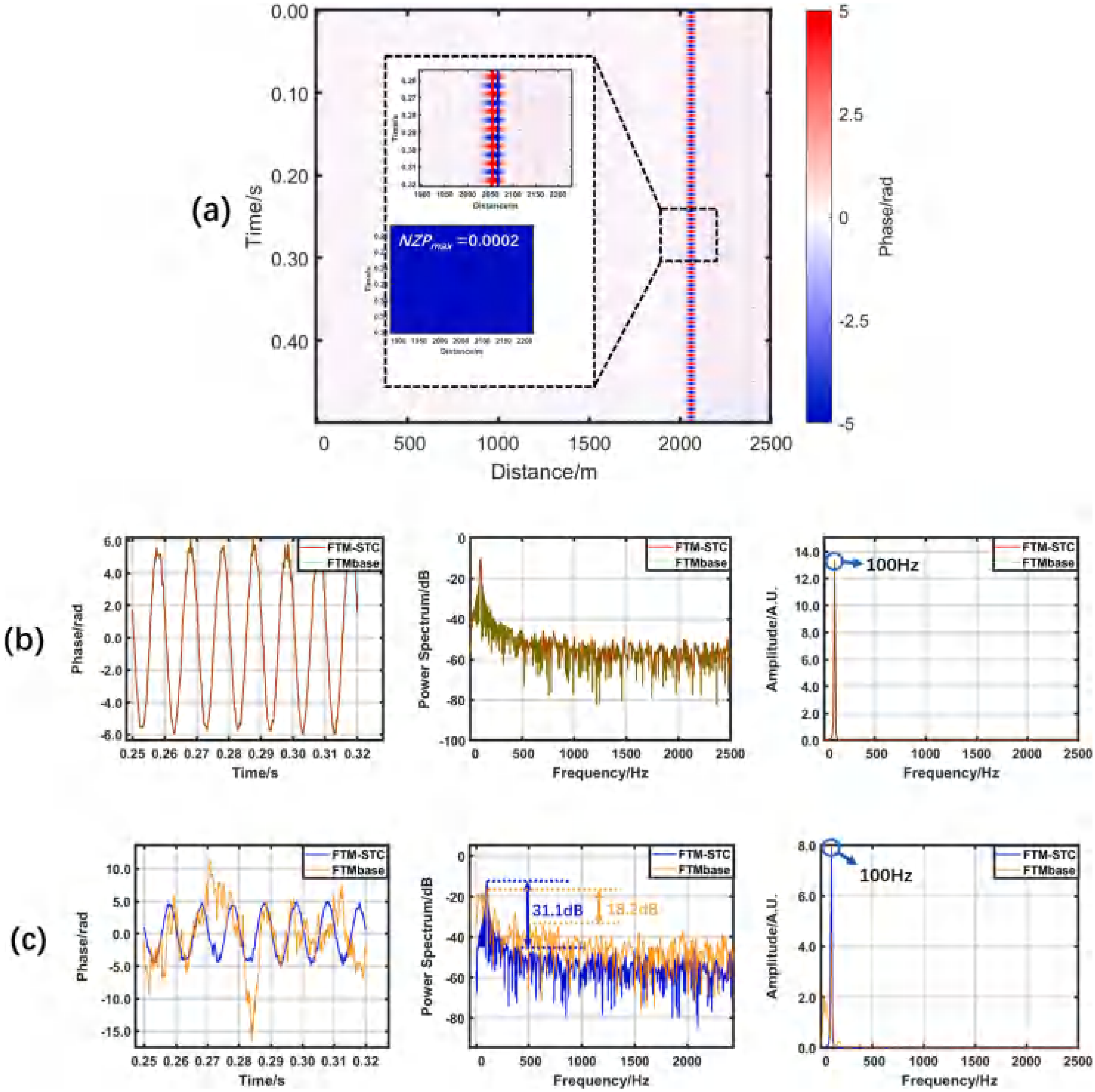

Fig. 16. Demodulation results of FTM-STPC when 100 Hz sinusoidal vibration is applied. (a) waterfall plot with fading suppression; (b) the temporal waveform plot, PSD plot, and frequency spectrum at 2052 m position before (FTMbased) and after (FTM-STPC) phase compensation; (c) the temporal waveform plot, PSD plot, and frequency spectrum at 2062 m position before (FTMbased) and after (FTM-STPC) phase compensation.

FTM for the first time. Unlike traditional digital phase demodulation methods, FTM eliminates the need for generating orthogonal components and relying on matched digital time-domain filters. Through rigorous derivation, we demonstrate that FTM achieves adaptive fast demodulation and filtering by filtering out conjugate terms in the frequency domain and performing subsequent frequency shifting. This method only results in a loss of half of the intensity value, while fully preserving the phase signal. Although the FTM method provides faster processing compared to traditional I/Q demodulation techniques, real-time implementation in systems with very high data rates or long data acquisition times may still face challenges in terms of computational complexity. Further optimization of the algorithm, possibly through parallel processing or hardware acceleration, could be explored to reduce the computational overhead in such scenarios. Moreover, our research delves into the mechanisms of fading noise, allowing precise localization and quantitative characterization of fading points. Ultimately, employing STPC enables effective fading noise suppression across the majority of fading regions. Compared with existing Φ-OTDR fading noise suppression techniques, precise localization of unreliable phase points can be achieved by detecting residues in wrapped phases. Subsequently, utilizing STPC on this basis enables the suppression of fading noise without sacrificing signal quality. By calculating the pre-compensation and post-compensation NZP_{max} values, the adequacy of fading suppression can be accurately measured. STPC is executed iteratively to refine the phase signal and can be independently integrated with various techniques, such as digital I/Q phase demodulation. Additionally, since the phase at the fading points is replaced with the phase from surrounding points, when the overall SNR is low, the phase used for replacement becomes random. After several iterations, the vibration phase signal may evolve into smooth random phase noise.

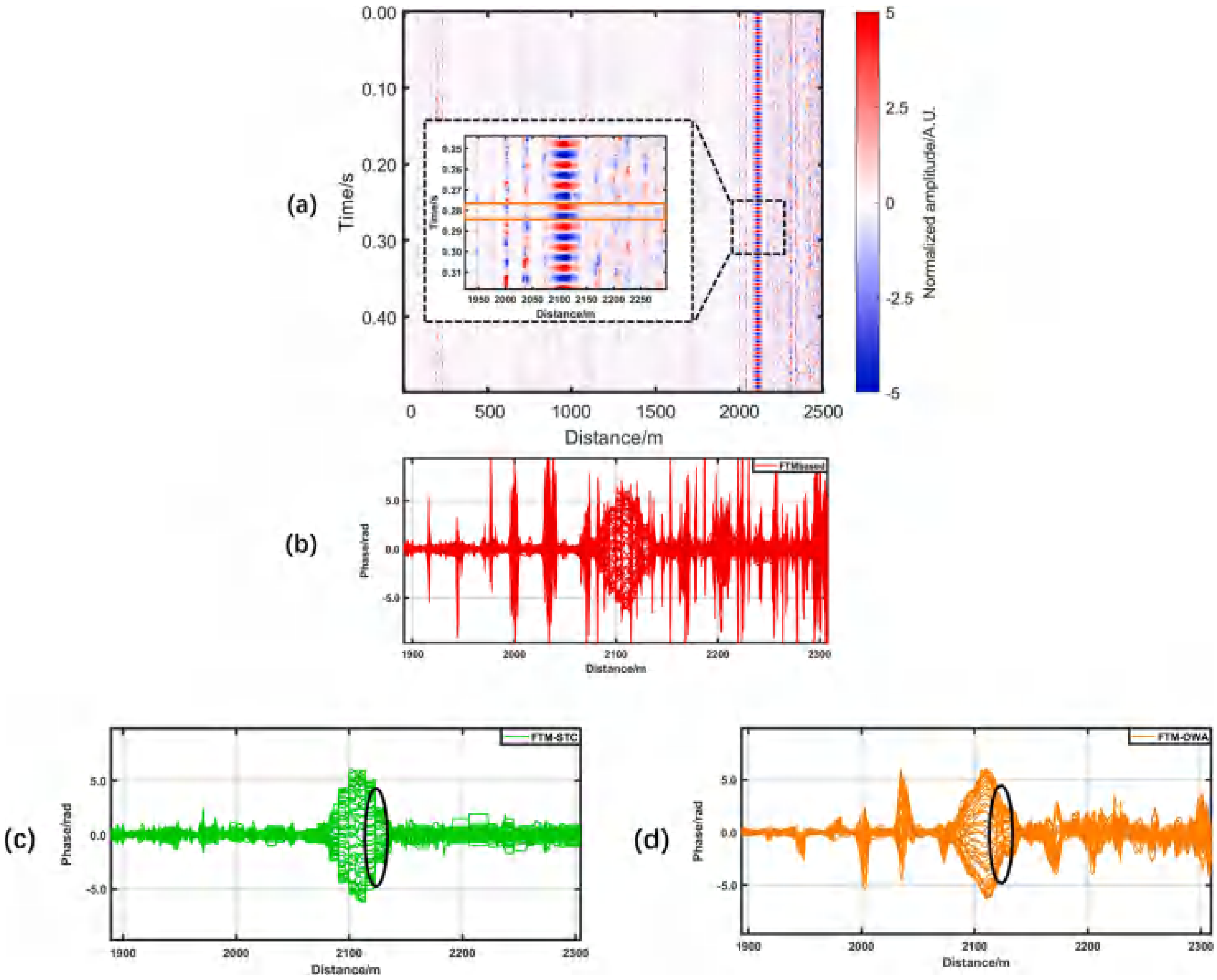

Fig. 17. (a) Waterfall plot of FTM phase demodulation with OWA fading noise suppression; (b) phase distribution from 0.275 s to 0.285 s without fading suppression; (c) phase distribution from 0.275 s to 0.285 s with STPC fading suppression; (d) phase distribution from 0.275 s to 0.285 s with OWA fading noise suppression.

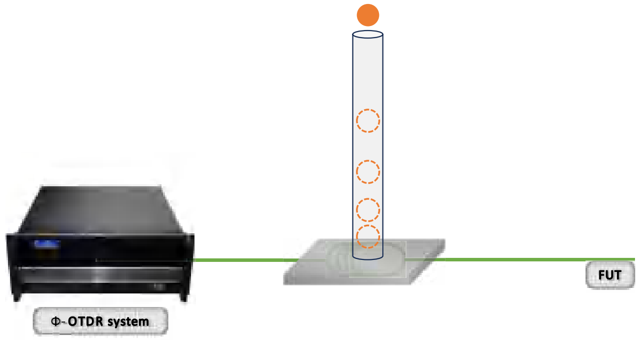

Fig. 18. Experimental setup for ping-pong ball underdamped vibration.

Therefore, noise suppression of the overall random phase prior to applying the STPC algorithm is an effective improvement. For large-strain vibration signals, where the phase difference between adjacent points exceeds π, the STPC algorithm is not applicable. Specifically, these points are recognized as residual points, and replacing them with nearby phase values fails to optimize the signal. This is why, in the presence of significant random phase noise, NZP_{max} cannot be reduced to 0, regardless of the number of iterations.

6. Conclusion

In conclusion, this study introduces the FTM-STPC algorithm, an innovative digital phase demodulation technique for heterodyne Φ-OTDR systems that seamlessly integrates fading noise suppression within the demodulation process. By employing frequency domain processing, FTM-STPC simplifies the system architecture, eliminating the need for orthogonal signal generation and digital time-domain filters. The algorithm enhances phase signal fidelity through adaptive filtering and accurately identifies fading points using residue detection, followed by STPC to mitigate noise under challenging conditions. Comprehensive simulations and experimental validations demonstrate that FTM-STPC significantly outperforms traditional digital I/Q phase demodulation methods in terms of demodulation speed, accuracy, and noise resistance, while maintaining fading noise suppression below 1 %. Overall, FTM-STPC offers a robust and efficient solution for enhancing the performance of heterodyne Φ-OTDR systems, paving the way for broader applications in various fields.

CRediT authorship contribution statement

Hao Ding: Writing – original draft, Visualization, Validation, Supervision, Software, Methodology, Conceptualization. **Xuping Zhang:** Supervision, Funding acquisition. **Shaoxiong Tang:** Validation, Software, Investigation. **Qiming Deng:** Validation, Software, Investigation.

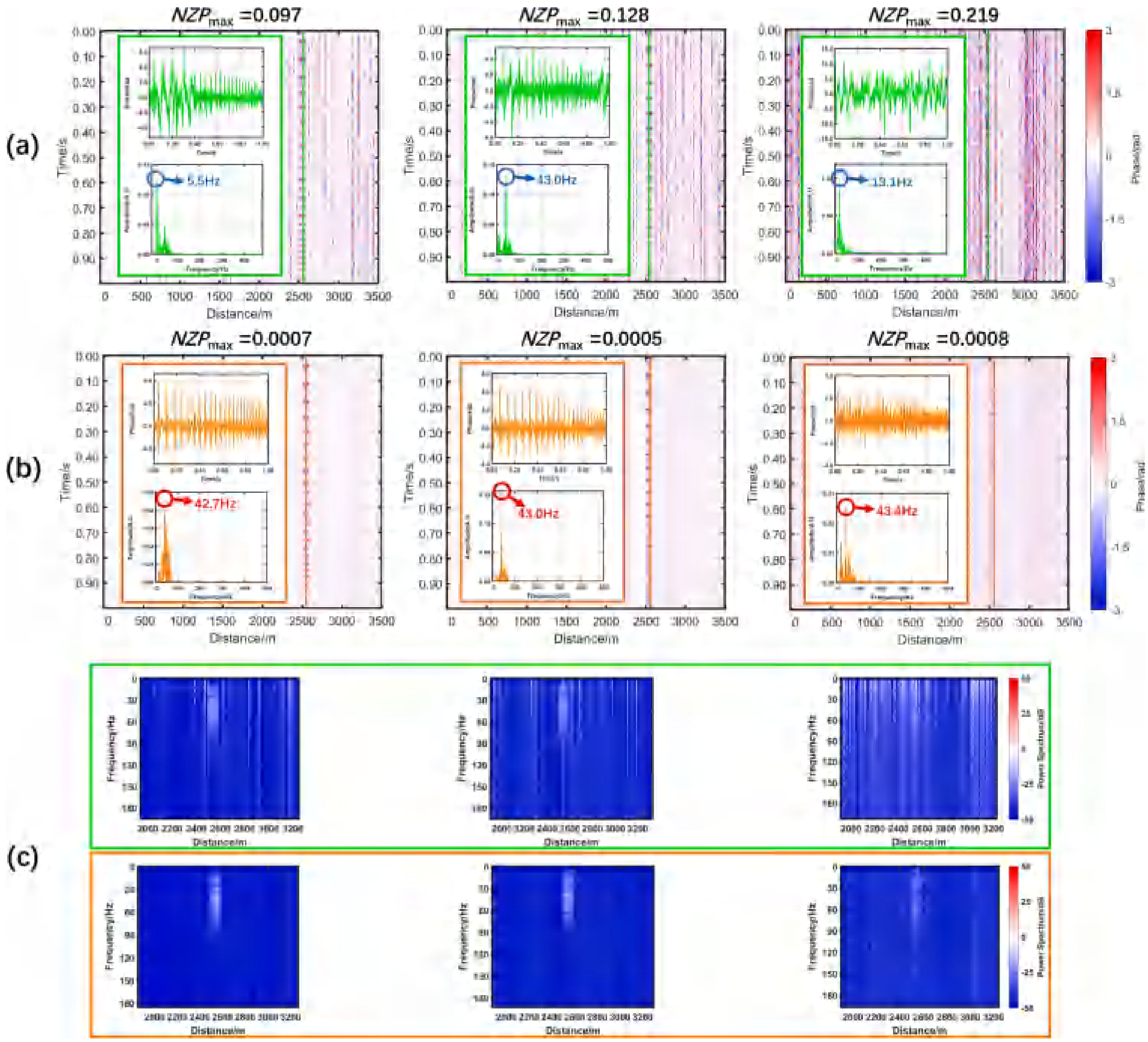

Fig. 19. Underdamped vibration demodulation results for a ping-pong ball. Each row corresponds to EDFA current settings of 65 mA, 60 mA, and 55 mA, from left to right. (a) FTM phase demodulation results: the upper subfigures show temporal waveform plots at 2580 m, and the lower subfigures display the corresponding frequency spectrum. (b) FTM-STPC phase demodulation results: the upper subfigures show temporal waveform plots at 2580 m, and the lower subfigures display the corresponding frequency spectrum. (c) PSD two-dimensional heatmaps from 1900 m to 3200 m before compensation (green box) and after compensation (orange box).

Chi Zhang: Visualization, Validation, Investigation. **Shuai Tong:** Validation, Formal analysis. **Yixin Zhang:** Writing – review & editing, Supervision, Methodology, Funding acquisition. **Huanhuan Liu:** Writing – review & editing, Validation, Conceptualization. **Fei Xiong:** Validation, Investigation. **Ningmu Zou:** Writing – review & editing, Supervision, Resources.

Declaration of competing interest

The authors declare that they have no known competing financial interests or personal relationships that could have appeared to influence the work reported in this paper.

Acknowledgments

This work was supported by National Natural Science Foundation of China (NSFC) under Grant (62175100); Fundamental Research Funds for the Central Universities (2024300447, 0213-14380264, 0213-14380265, 4830-16003302); General Program of Shenzhen Science, Technology & Innovation Commission (JCYJ20220530113811026); Shenzhen Research Foundation under Grant (KJZD20230923114601003); CAS Pioneer Hundred Talents Program; Shenzhen Science and Technology Program (JSGGKQTD20221101115656030).

Data availability

Data will be made available on request.

References

[1] H.F. Taylor, C.E. Lee, Apparatus and method for fiber optic intrusion sensing[J], 1993.

[2] X. Zhang, Z. Ding, R. Hong, et al., Phase sensitive optical time-domain reflective distributed optical fiber sensing technology[J], Guangxue Xuebao 41 (1) (2021) 0106004.

[3] A. Masoudi, M. Belal, T.P. Newson, A distributed optical fiber dynamic strain sensor based on phase-OTDR[J], Meas. Sci. Technol. 24 (8) (2013) 085204.

[4] W. Chen, J. Jiang, S. Wang, et al., Hybrid demodulation method for distributed acoustic sensing based on coherent detection and pulse pair[J], Appl. Phys Express 13 (1) (2019) 012012.

[5] A.E. Alekseev, V.S. Vdovenko, B.G. Gorshkov, et al., A phase-sensitive optical time-domain reflectometer with dual-pulse diverse frequency probe signal[J], Laser Phys. 25 (6) (2015) 065101.

[6] G. Fang, T. Xu, S. Feng, et al., Phase-sensitive optical time domain reflectometer based on phase-generated carrier algorithm[J], J. Lightwave Technol. 33 (13) (2015) 2811–2816.

[7] X. He, S. Xie, F. Liu, et al., Multi-event waveform-retrieved distributed optical fiber acoustic sensor using dual-pulse heterodyne phase-sensitive OTDR[J], Opt. Lett. 42 (3) (2017) 442–445.

[8] A.E. Alekseev, V.S. Vdovenko, B.G. Gorshkov, et al., Phase-sensitive optical coherence reflectometer with differential phase-shift keying of probe pulses[J], Quantum Electron. 44 (10) (2014) 965.

[9] H.F. Martins, K. Shi, B.C. Thomsen, et al., Real time dynamic strain monitoring of optical links using the backreflection of live PSK data[J], Opt. Express 24 (19) (2016) 22303–22318.

[10] C. Zhang, N.M. Zou, J.Y. Song, et al., Digital signal processing and application of Φ-OTDR system[J], Opto-Electron Eng 50 (2) (2023) 220088.

[11] X.P. Zhang, Y.X. Zhang, L. Wang, et al., Current status and future of research and applications for distributed fiber optic sensing technology[J], Acta Opt. Sin. 44 (1) (2024) 0106001.

[12] Z. Pan, K. Liang, Q. Ye, et al., Phase-sensitive OTDR system based on digital coherent detection[C], in: 2011 Asia Communications and Photonics Conference and Exhibition (ACP). IEEE, 2011, pp. 1-6.

[13] Z. Wang, L. Zhang, S. Wang, et al., Coherent Φ-OTDR based on I/Q demodulation and homodyne detection[J], Opt. Express 24 (2) (2016) 853–858.

[14] D. Chen, Q. Liu, X. Fan, et al., Distributed fiber-optic acoustic sensor with enhanced response bandwidth and high signal-to-noise ratio[J], J. Lightwave Technol. 35 (10) (2017) 2037–2043.

[15] G. Yang, X. Fan, S. Wang, et al., Long-range distributed vibration sensing based on phase extraction from phase-sensitive OTDR[J], IEEE Photonics J. 8 (3) (2016) 1–12.

[16] S. Liu, F. Yu, L. Shao, et al., Fast phase demodulation method for heterodyne phase-sensitive OTDR[C], in: 2022 Asia Communications and Photonics Conference (ACP). IEEE, 2022, pp. 157–159.

[17] Y. Wu, Z. Wang, J. Xiong, et al., Interference Fading Elimination with Single Rectangular Pulse in Φ-OTDR[J], J. Lightwave Technol. 37 (13) (2019) 3381–3387.

[18] H. Li, T. Liu, C. Fan, et al., Fading suppression for distributed acoustic sensing assisted with dual-laser system and differential-vector-sum algorithm[J], IEEE Sens. J. 22 (10) (2022) 9417–9425.

[19] X. He, X. Xu, M. Zhang, et al., On the phase fading effect in the dual-pulse heterodyne demodulated distributed acoustic sensing system[J], Opt. Express 28 (22) (2020) 33433–33447.

[20] M. Zabihi, Y. Chen, T. Zhou, et al., Continuous fading suppression method for Φ-OTDR systems using optimum tracking over multiple probe frequencies[J], J. Lightwave Technol. 37 (14) (2019) 3602–3610.

[21] Y. Wang, Y. Li, L. Xiao, et al., Interference fading suppression using active frequency transformation method with auxiliary interferometer feedback[J], J. Lightwave Technol. 40 (3) (2022) 872–879.

[22] C. Dorize, S. Guerrier, E. Awwad, et al., Identification of Rayleigh fading induced phase artifacts in coherent differential Φ-OTDR[J], Opt. Lett. 46 (11) (2021) 2754–2757.

[23] Z. Zhao, H. Wu, J. Hu, et al., Interference fading suppression in φ-OTDR using space-division multiplexed probes[J], Opt. Express 29 (10) (2021) 15452–15462.

[24] G. Tu, M. Zhao, Z. Tang, et al., Fading noise suppression in Φ-OTDR based on nearest neighbor analysis[J], J. Lightwave Technol. 38 (23) (2020) 6691–6698.

[25] Y. Lu, X. Hu, Z. Yu, et al., Fading noise reduction in distributed acoustic sensing using an optimal weighted average algorithm[J], Appl. Opt. 60 (34) (2021) 10643–10648.

[26] T. Li, F. Zhang, J. Lin, et al., Fading noise suppression method of Φ-OTDR system based on non-local means filtering[J], Opt. Fiber Technol. 81 (2023) 103572.

[27] S. Tong, X. Zhao, C. Zhang, et al., Research on PFN suppression methods in φ-OTDR systems based on the MSI-VPFN algorithm[J], Opt. Express 32 (26) (2024) 47123–47136.

[28] P. Wang, N. Xu, Y. Wang, et al., Multiresolution phase compensation for phase-sensitive OTDR[J], IEEE Sens. J. 22 (15) (2022) 14937–14943.

[29] M. Sun, M. Yu, H. Wang, et al., Fading discrimination and suppression of Φ-OTDR system based on FAM-MAE[J], IEEE Sens. J. (2023).

[30] X. Zhang, Q. Wang, F. Xiong, et al., Performance enhancement method for phase-sensitive optical time-domain reflectometer system based on suppression of fading induced false alarms, Opt. Eng. 59 (04) (2020) 46101.

[31] F. Jiang, Z. Zhang, Z. Lu, et al., High-fidelity acoustic signal enhancement for phase-OTDR using supervised learning[J], Opt. Express 29 (21) (2021) 33467–33480.

[32] Y. Zhao, Y. Li, N. Wu, Distributed acoustic sensing vertical seismic profile data denoiser based on convolutional neural network[J], IEEE Trans. Geosci. Remote Sens. 60 (2020) 1–11.

[33] T.X. Li, F.D. Zhang, J. Lin, et al., Fading noise suppression method of Φ-OTDR system based on GA-VMD algorithm[J], IEEE Sens. J. (2023).

[34] T. Kreis, Digital holographic interference-phase measurement using the Fourier -transform method[J], JOSA A 3 (6) (1986) 847–855.

[35] R.M. Goldstein, H.A. Zebker, C.L. Werner, Satellite radar interferometry: two-dimensional phase unwrapping[J], Radio Sci. 23 (4) (1988) 713–720.

[36] D.C. Ghiglia, M.D. Pritt, Two-dimensional phase unwrapping: theory, algorithms, and software[M]. New York, Wiley, 1998.

[37] L. Zhao, X. Zhang, Z. Xu, A high-fidelity numerical model of coherent Φ-OTDR[J], Measurement 230 (2024) 114526.

[38] A. Hore, D. Ziou, Image quality metrics: PSNR vs. SSIM[C]//2010 20th international conference on pattern recognition. IEEE, 2010: 2366-2369.